AIAA JOURNAL
Vol. 34, No. 4, April 1996

Grid Influence on Upwind Schemes for the Euler and Navier–Stokes Equations

X. D. Zhang,* J.-Y. Trépanier,† M. Reggio,‡ A. Benmeddour,§ and R. Camarero¶
École Polytechnique de Montréal, Montréal, Québec H3C 3A7, Canada

The grid influence on the standard Roe's upwind scheme in two space dimensions is investigated. It is shown that inaccurate solutions can be obtained even in smooth flow regions and even with regularly structured triangular meshes. Some numerical analyses and various inviscid and viscous computations are conducted to provide a better understanding of this behavior. High-order reconstructions together with the standard scheme are shown to give only limited improvements. A grid-independent upwind scheme based on a five-wave model has been tested and has shown some potential in improving the situation.

I. Introduction

GODUNOV type methods[1] have played an important role in the development of upwind schemes. The approximate Riemann solver proposed by Roe[2] has led this approach to a practical level in which the Riemann problem of the Euler equations is linearized locally and solved exactly in an average state. The beauty and efficiency of this method found in one-dimensional problems, however, are diminished when applied directly to two- or three-dimensional situations since the simple wave model is based on local one-dimensional Riemann problem. As a result, for first-order schemes, the numerical solutions are smeared and are highly grid dependent.

During the last decade, many theoretical and numerical investigations have been carried out to improve the situation. A first type of approach uses local mesh adjustment, especially across discontinuities such as shocks, so that the propagating direction of the dominant wave is coincident with the mesh orientation. By doing so, the local discontinuities are correctly represented by the one-dimensional Riemann problem and, in some cases, this approach works very well.[3–5] However, the efficiency of the grid adaptation may be a serious issue, and it is not clear how to adjust the grid in smooth flow regions.

A second avenue using high-order reconstruction (HOR) has been investigated systematically by Yee[6] using a total variation diminishing (TVD) scheme for structured meshes and by Barth[7] for unstructured meshes. As expected, HOR can reduce the numerical dissipation introduced by first-order upwinding and the one-dimensional Riemann solver. However, numerical analysis[8] has shown that this kind of improvement is limited to, at most, second-order accuracy. Numerical experiences as reported by Aftosmis et al.,[9] as well as in the present paper, demonstrated that it is still grid dependent. It is felt that by only increasing the order of the scheme, one can seldom remove or reduce significantly the grid dependency and the numerical dissipation.

The third approach is the multidimensional upwind method that is based more deeply on the physical aspects of the Euler equations. Several efforts have been made in this direction. Among them, rotated upwind methodology solves the Riemann problem in the direction of the local flow or pressure gradient[10–13]; the simple wave model decomposes the total flux into several parts, each of them being contributed by a simple wave with its own strength and propagating direction[14–16] and characteristic theory-based advection scheme diagonalizes the Euler equations to a set of compatibility equations corresponding to physically relevant characteristic surfaces depending on the local flow.[17–19] Although it is not clear which of the approaches is closer to the underlying physics, numerical investigations[20] have shown that none of these approaches have yet reached a satisfactory level with respect to their accuracy and robustness.

One typical case of the grid dependency has been reported by Barth and Jespersen[21] (see Fig. 4.1, Ref. 21) in which a viscouslike unphysical Euler solution was observed. It was demonstrated by the authors[21] that the second-order scheme can improve this kind of unphysical behavior. With different grids, our experience shows that it can seldom be removed completely even with a high-order scheme. By realizing the importance of the geometric factors that contributed to the grid dependency of the scheme, Barth[7] has further proposed a containment sphere concept to improve the situation. Despite its limitation to cell-vertex schemes, however, the redesigned control volume based on the containment sphere tessellation may still suffer from irregular interface orientations for irregular unstructured meshes.

The objective of the present work is to investigate the influence of the grid on the solution accuracy of two-dimensional Euler and Navier–Stokes equations when the conventional upwind scheme of Roe[2] is used, to try to provide better understandings of the unphysical behavior, and to show the possible improvements in solution accuracy by using one of the simplest grid-independent approaches as proposed by Rumsey et al.[12] The influence of the grid aspect ratio and the unstructured grid regularity are also investigated. The main concern of the present study is the grid related solution accuracy in smooth flow regions.

II. Governing Equations

The compressible laminar Navier–Stokes equations can be written in the following matrix form:

$$U_t + \nabla \cdot (\mathcal{F} - \mathcal{G}) = 0 \tag{1}$$

where U is the vector of conservative variables and $\mathcal{F}$ and $\mathcal{G}$ are the inviscid and viscous flux matrices, respectively. When an inviscid flow is concerned, the viscous flux matrix $\mathcal{G}$ is set to zero. In a two-dimensional Cartesian coordinate system, the matrices are given by

$$U = (\rho, \rho u_x, \rho u_y, \rho e)^\tau$$

Presented as Paper 95-0347 at the AIAA 34th Aerospace Sciences Meeting, Reno, NV, Jan. 9–13, 1995; received April 5, 1995; revision received Oct. 6, 1995; accepted for publication Oct. 9, 1995.

*Research Professional, Centre de Recherche en Calcul Appliqué and Department of Mechanical Engineering, C.P. 6079, Succ. Centre-Ville.

†Assistant Professor, Centre de Recherche en Calcul Appliqué and Department of Mechanical Engineering, C.P. 6079, Succ. Centre-Ville. Member AIAA.

‡Associate Professor, Centre de Recherche en Calcul Appliqué and Department of Mechanical Engineering, C.P. 6079, Succ. Centre-Ville.

§Ph.D. Student, Centre de Recherche en Calcul Appliqué and Department of Mechanical Engineering, C.P. 6079, Succ. Centre-Ville.

¶Professor, Centre de Recherche en Calcul Appliqué and Department of Mechanical Engineering, C.P. 6079, Succ. Centre-Ville.

$$\mathcal{F} = \begin{pmatrix} \rho u_x & \rho u_y \\ \rho u_x u_x + p & \rho u_y u_x \\ \rho u_x u_y & \rho u_y u_y + p \\ \rho u_x e + u_x p & \rho u_y e + u_y p \end{pmatrix}$$

$$\mathcal{G} = \begin{pmatrix} 0 & 0 \\ \sigma_{xx} & \sigma_{xy} \\ \sigma_{yx} & \sigma_{yy} \\ \sigma_{xx}u_x + \sigma_{xy}u_y + q_x & \sigma_{yx}u_x + \sigma_{yy}u_y + q_y \end{pmatrix}$$

where ρ is the density, $\boldsymbol{u} = (u_x, u_y)^\tau$ the fluid velocity vector, e the specific total energy, p the static pressure, and τ the transpose. Based on Stokes' hypothesis, the components of the viscous stress tensor and the heat flux vector $\boldsymbol{q} = (q_x, q_y)^\tau$ are given as follows:

$$\sigma_{xx} = \frac{\mu}{Re}\left(\frac{4}{3}\frac{\partial u_x}{\partial x} - \frac{2}{3}\frac{\partial u_y}{\partial y}\right)$$

$$\sigma_{xy} = \sigma_{yx} = \frac{\mu}{Re}\left(\frac{\partial u_x}{\partial y} + \frac{\partial u_y}{\partial x}\right)$$

$$\sigma_{yy} = \frac{\mu}{Re}\left(\frac{4}{3}\frac{\partial u_y}{\partial y} - \frac{2}{3}\frac{\partial u_x}{\partial x}\right)$$

$$q_x = -\frac{\mu\gamma}{PrRe(\gamma - 1)}\frac{\partial T}{\partial x}$$

$$q_y = -\frac{\mu\gamma}{PrRe(\gamma - 1)}\frac{\partial T}{\partial y}$$

where T is the static temperature, $\gamma = c_p/c_v$ the ratio of the specific heats of the fluid, μ the molecular viscosity normalized by the value at stagnation point μ_0, Re the Reynolds number based on the stagnation properties, and Pr the Prandtl number. The equation system (1) is completed by introducing the equation of state that for a perfect gas is

$$p = \rho T = (\gamma - 1)\rho\left[e - \tfrac{1}{2}\left(u_x^2 + u_y^2\right)\right] \tag{2}$$

where μ is a function of the temperature T as given by Sutherland's law

$$\mu = T^{\frac{3}{2}}[(1 + S_0)/(T + S_0)] \tag{3}$$

in which $S_0 = S_1/T_0$ is a constant, with $S_1 = 110$ K for air and T_0 the stagnation temperature.

III. Numerical Algorithm

Flux Discretization

One of the widely used schemes for compressible flow computations is Roe's flux-difference scheme.[2] The key feature of this scheme is the introduction of an averaged state $\bar{A}$ to approximate the Jacobian $\mathcal{A} = \partial \boldsymbol{F}/\partial \boldsymbol{U}$ on each interface. This averaged matrix $\bar{A}$ can be expressed as

$$\bar{A} = \mathcal{Q}\mathcal{D}\mathcal{Q}^{-1}$$

where $\mathcal{D}$ is a diagonal matrix formed by the four eigenvalues $\lambda_{1,2,3,4}$ and $\mathcal{Q}$ is formed by the corresponding independent four eigenvectors $\boldsymbol{e}_{1,2,3,4}$ of $\bar{A}$.

In the standard extension of Roe's scheme from one-dimensional[2] to two-dimensional problems (for example, see Ref. 22), the flux vector on any interface with right and left states represented by R and L is computed by

$$\boldsymbol{F} = \tfrac{1}{2}(\boldsymbol{F}_R + \boldsymbol{F}_L) - \tfrac{1}{2}\mathcal{Q}|\mathcal{D}|\mathcal{Q}^{-1}(\boldsymbol{U}_R - \boldsymbol{U}_L) \tag{4}$$

In the present work, a cell-centered scheme is used, i.e., all of the variables are stored at each triangle center and the triangle itself is chosen as the control volume. The method selected to evaluate the right and left states at a given interface in Eq. (4) determines the order of the scheme. Piecewise constant approximation on each triangle leads to a first-order scheme. A second-order scheme can be obtained by using piecewise-linear reconstruction within the triangle.[21] A third-order scheme can be constructed by using quadratic reconstruction and by using two-point Gauss quadrature to integrate the flux.[23]

The gradient of a variable ϕ is first computed at each vertex of the unstructured triangular grid by the application of Gauss theorem to its median dual V that is formed from median segments connecting the triangular centroid and the face midpoints:

$$\nabla\phi = \frac{1}{V}\oint_{\partial V}\phi \boldsymbol{n}_v \,\mathrm{d}s = \frac{1}{V}\sum_{n(c)}\phi \boldsymbol{s} \tag{5}$$

where $\boldsymbol{n}_v$ is the unit outward normal vector of V, $n(c)$ its number of sides, and $\boldsymbol{s}$ the facial length of V with the direction of $\boldsymbol{n}_v$. Then, the gradient in each triangle (cell value) is obtained from an arithmetical mean of its three vertex values and the piecewise-linear reconstruction within each triangle for the conservative variable Φ is given by[21]

$$\Phi(x, y) = \Phi_0 + \Delta\boldsymbol{r}^\tau \nabla\Phi_0 \tag{6}$$

The quadratic reconstruction has been realized using a least-square technique to evaluate the gradient and the second-order derivatives. The quadratic reconstruction is then given as[23]

$$\Phi(x, y) = \Phi_0 + \Delta\boldsymbol{r}^\tau \nabla\Phi_0 + \tfrac{1}{2}\Delta\boldsymbol{r}^\tau H_0 \Delta\boldsymbol{r} \tag{7}$$

where

$$H_0 = \begin{pmatrix} \dfrac{\partial^2 u}{\partial x^2} & \dfrac{\partial^2 u}{\partial x \partial y} \\ \dfrac{\partial^2 u}{\partial x \partial y} & \dfrac{\partial^2 u}{\partial y^2} \end{pmatrix}$$

is the Hessian matrix.

The quadratic reconstruction is made k exact by using an approach proposed by Barth and Frederickson[24] that increases the physical support used. The gradient and the Hessian matrix are directly evaluated at the cell center with a stencil comprising all of the neighboring triangles that share at least one node with the considered triangle. This stencil will generally provide enough support (more than five) even at the boundaries.

To preserve the monotonicity of the scheme using HOR, a proper limiter needs to be defined. In this paper, both limiters defined by Barth and Jesperson[21] and Venkatakrishnan[25] are used, whereas most of the numerical computations are conducted using Venkatakrishnan's limiter because of its superior convergence properties.

The viscous fluxes are evaluated by computing the gradient at the edges as an area (of the median dual) weighted averaging of the gradient previously computed at the vertices, as just described.

Boundary Conditions

The flow boundary conditions are imposed using fictitious cells outside the boundaries. The flow properties are set in these cells so as to represent the various types of boundary conditions. Then the Riemann solver is applied regularly to the boundary interface giving the required fluxes. On inlet or outlet boundaries, the number of conditions imposed depends on the local Mach number. For example, for a supersonic outlet, all external fictitious cell values are extrapolated from internal values, whereas for a subsonic outlet, the back pressure is imposed and other properties are extrapolated. The isentropic infinite conditions are imposed on far-field boundaries. On solid walls, the flow properties in the fictitious cells are reflected according to inviscid or viscous boundary conditions. The adiabatic wall condition is used for temperature.

For viscous flow computations, an accurate gradient evaluation in Eq. (5) on solid boundary nodes can be achieved by reflecting the contribution of the internal integration to the outside part. Details can be found in Ref. 26.

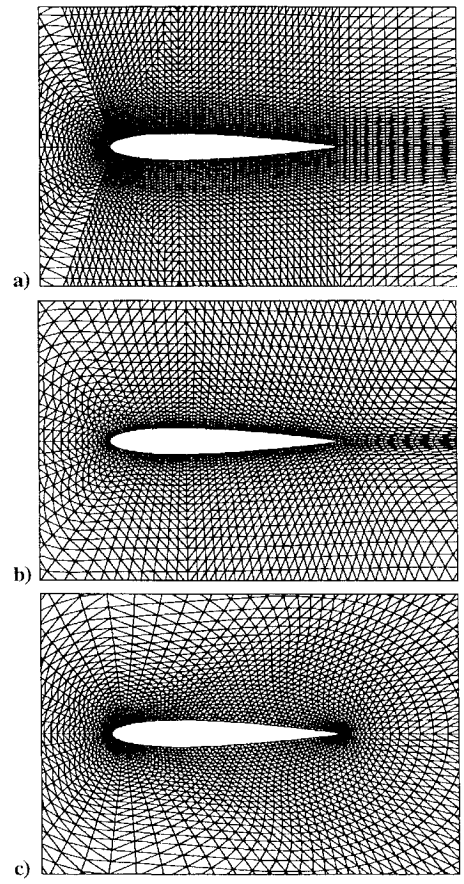

Fig. 1 Different computational triangular grids for the NACA0012 test case: a) GE_{-1}, b) GE_{-2}, and c) GE_{-3}.

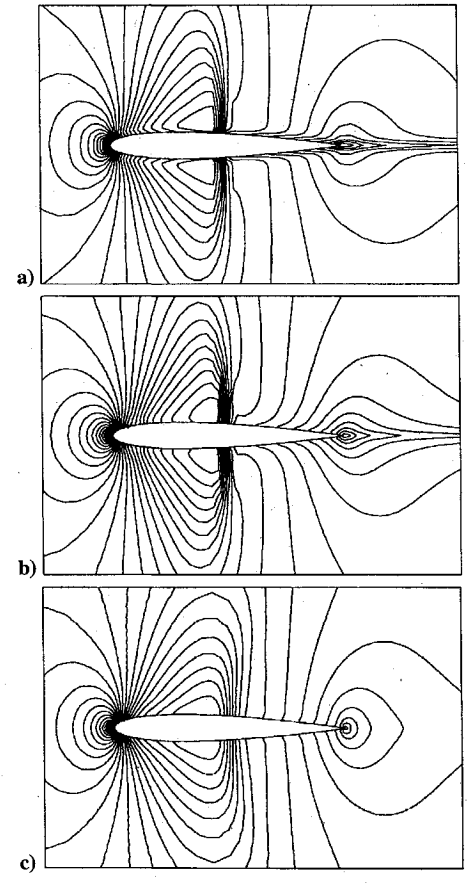

Fig. 2 Computed Mach contours using first-order scheme with different grids: a) GE_{-1}, b) GE_{-2}, and c) GE_{-3}.

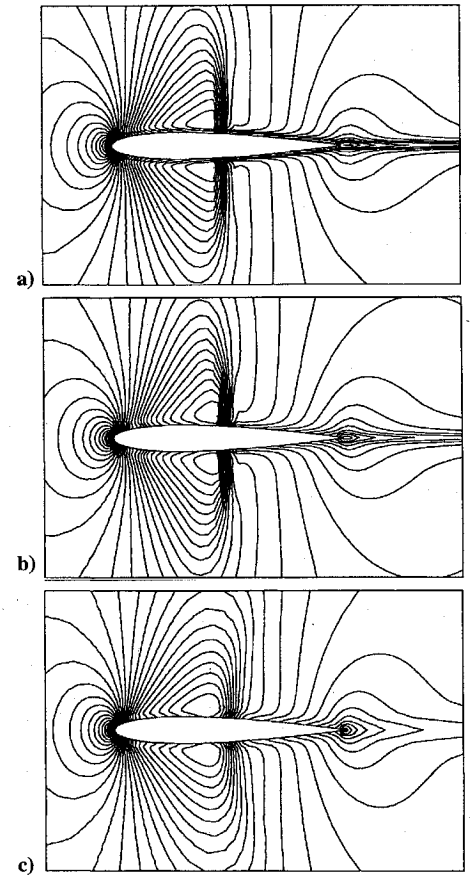

Fig. 3 Computed temperature contours using first-order scheme with different grids: a) GE_{-1}, b) GE_{-2}, and c) GE_{-3}.

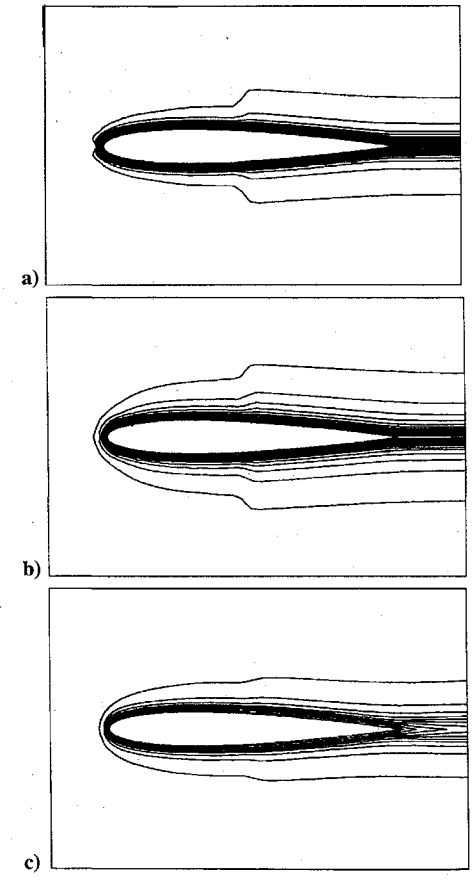

Fig. 4 Computed entropy contours using first-order scheme with different grids: a) GE_{-1}, b) GE_{-2}, and c) GE_{-3}.

Solution Procedure

Once the inviscid and viscous fluxes are all calculated, the conservative properties U are advanced explicitly to the next time level $(n+1)$ by

$$U_p^{n+1} = U_p^n - \frac{\Delta t}{\text{area}} \sum_{k=1}^{3} \left(F_k^n - G_k^n\right) S_k \tag{8}$$

where S_k is the length of the kth side of the triangular control volume. Since the calculations conducted in this paper are all steady cases, the time-accurate explicit scheme is time consuming. However, a local time stepping technique proposed by Zhang et al.[27] is used to accelerate the convergence. Furthermore, a multigrid acceleration procedure for unstructured meshes, as discussed by Currie,[28] is used for the time integration. As a result, the Courant–Fredrichs–Lewy (CFL) number used for the computations can be chosen as $c = 1.9$.

IV. Grid Influence

A theoretical analysis about the grid influence using Riemann solvers for a linear advection equation in two-dimensions can be found in Ref. 8. In this study, various high-order polynomial reconstructions are analyzed from a mathematical point of view and the conclusions for triangular meshes are as follows.

1) First-order schemes (i.e., piecewise constant) do not satisfy the consistency condition.

2) Second-order schemes (i.e., piecewise linear) with zero-mean HOR have only first-order spatial accuracy; with nonzero-mean HOR, second-order spatial accuracy can be achieved only when regular meshes are used.

3) Third-order spatial accuracy cannot be achieved, no matter the order of the reconstruction and the number of Gaussian points used.

4) Zero cross diffusion is achieved only when regular meshes are used.

From these conclusions, it seems that the first-order scheme should be abandoned, that a high-order scheme is needed, and that a scheme higher than third-order is unnecessary. Now, the remaining question is: will a high-order scheme be accurate and efficient enough to provide satisfactory results without specific attention to the grid? Seeking an absolutely grid-independent scheme may not be practical, but the grid dependency must be small enough for an acceptable scheme. However, some simple numerical test cases presented in this paper provide some bad examples for the standard Roe's upwind scheme that has been widely used together with HOR.

One of the main drawbacks for the approximate Riemann solver is the uncertainty of the upwind direction that should be independent of the grid orientation. This may become clearer after the following discussion.

The Euler flux evaluation formula of Roe's scheme (4) can be rewritten as

$$F = \frac{1}{2}(F_R + F_L) - \frac{1}{2}\sum_{k=1}^{4} |\lambda_k| \alpha_k e_k \tag{9}$$

where the second term in the right-hand side (RHS) represents the interaction of all of the physical waves at the cell interface as a superposition of four simple waves with

$$\begin{aligned} e_1 &= (1, \tilde{u}_x + \tilde{c}\cos\theta, \tilde{u}_y + \tilde{c}\sin\theta, \tilde{H} + \tilde{c}\tilde{u}_\parallel)^\tau \\ e_2 &= (1, \tilde{u}_x - \tilde{c}\cos\theta, \tilde{u}_y - \tilde{c}\sin\theta, \tilde{H} - \tilde{c}\tilde{u}_\parallel)^\tau \\ e_3 &= (0, -\tilde{c}\sin\theta, \tilde{c}\cos\theta, \tilde{c}\tilde{u}_\perp)^\tau \\ e_4 &= \left[1, \tilde{u}_x, \tilde{u}_y, \tfrac{1}{2}\left(\tilde{u}_x^2 + \tilde{u}_y^2\right)\right]^\tau \end{aligned} \tag{10}$$

corresponding to two acoustic waves, one shear wave and one entropy wave. The λ_k are their propagating speeds, which are given by

$$\lambda_1 = \tilde{u}_\parallel + \tilde{c}, \qquad \lambda_2 = \tilde{u}_\parallel - \tilde{c}, \qquad \lambda_3 = \tilde{u}_\parallel, \qquad \lambda_4 = \tilde{u}_\parallel$$

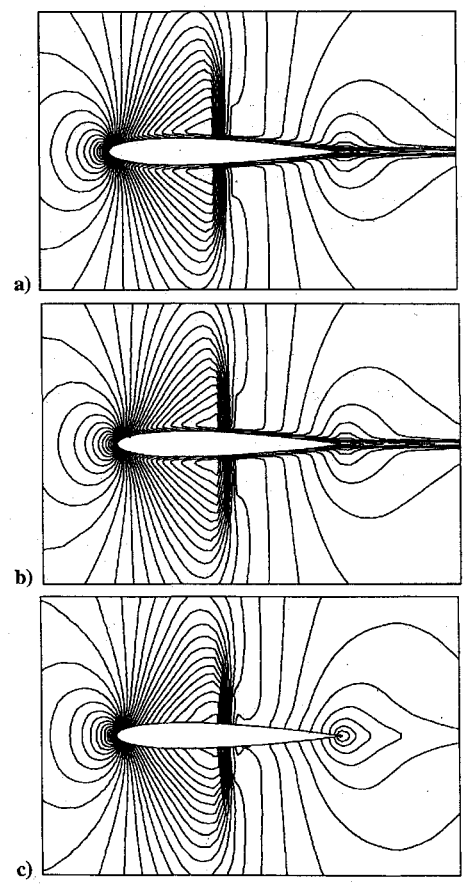

Fig. 5 Computed temperature contours using grid GE-$_1$ with different schemes: a) second-order scheme, b) third-order scheme, and c) rotated first-order scheme.

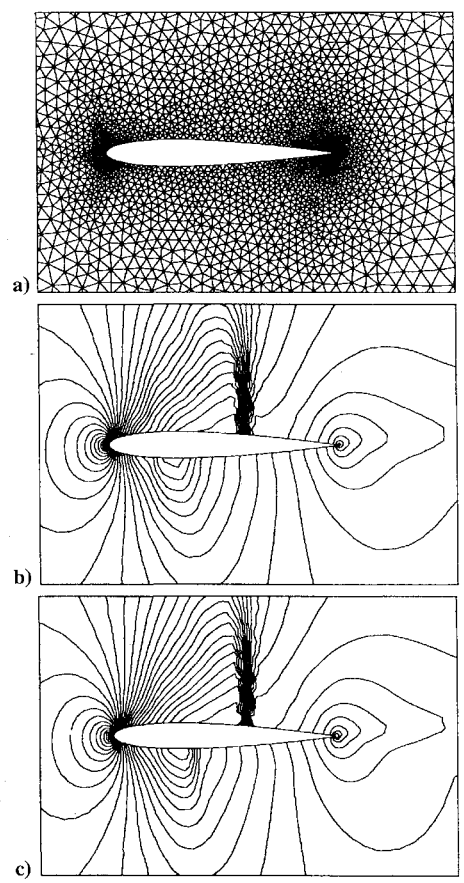

Fig. 6 Unstructured grid and computed temperature contours using standard schemes with $M_{inf} = 0.8$, $\alpha = 1.25$ deg: a) grid GE-$_{ust}$, b) first-order scheme, and c) second-order scheme.

and the α_k are their strengths, which have the following expressions:

$$\begin{aligned}\alpha_1 &= (1/2\tilde{c}^2)(\Delta p + \tilde{\rho}\tilde{c}\Delta u_{\parallel})\\ \alpha_2 &= (1/2\tilde{c}^2)(\Delta p - \tilde{\rho}\tilde{c}\Delta u_{\parallel})\\ \alpha_3 &= (1/\tilde{c})\tilde{\rho}\Delta u_{\perp}\\ \alpha_4 &= (1/\tilde{c}^2)(\tilde{c}^2\Delta\rho - \Delta p)\end{aligned} \tag{11}$$

with

$$\begin{aligned}\tilde{u}_{\parallel} &= \tilde{u}_x\cos\theta + \tilde{u}_y\sin\theta\\ \tilde{u}_{\perp} &= -\tilde{u}_x\sin\theta + \tilde{u}_y\cos\theta\\ \Delta u_{\parallel} &= \Delta u_x\cos\theta + \Delta u_y\sin\theta\\ \Delta u_{\perp} &= -\Delta u_x\sin\theta + \Delta u_y\cos\theta\end{aligned} \tag{12}$$

where θ is the angle that defines the upwinding direction and the tilde represents Roe's average value of the corresponding variables. If $\theta = \theta_g$, the angle of the grid normal direction, the wave model is the standard grid-aligned model. The choice of the direction θ directly affects the upwinding term in Eq. (9).

It is evident that the directions of the two acoustic waves $\boldsymbol{e}_{1,2}$ and the shear wave $\boldsymbol{e}_3$ are strongly dependent on the choice of θ but the entropy wave $\boldsymbol{e}_4$ is not. The physically correct direction should mainly consider these two types of waves. If the acoustic waves are dominant, corresponding to a large pressure difference, the direction based on the pressure gradient may be relevant, whereas if the shear wave becomes dominant, corresponding to a large velocity difference, then the direction based on the velocity difference may be appropriate. In fact, these are the basic ideas of the various rotated upwind algorithms,[10–13] and great improvements have been achieved especially across discontinuities using these approaches.

It is noted that in general flow patterns, the dominant wave is uncertain and it is unphysical to force every wave to propagate in the same direction. Allowing different waves to propagate in different directions[14,19] may be more physically sound. Further investigations need to be done along this direction. A disadvantage of rotated upwind schemes is their poor convergence performance because the upwinding direction depends on the local flow properties. Freezing the direction for some iterations[12] and blending between the computed direction and the grid face normal[13] are often used to improve the convergence. The additional parameters introduced in these techniques are difficult to control and are quite problem and grid dependent.

Considering the solution in smooth regions, especially the problem shown in Fig. 4.1 of Ref. 21, it seems that the misrepresentation of the shear wave is one of the major factors contributing to the grid dependency. In fact, shear waves are not represented properly by the standard four-wave model even if a rotated upwind scheme is used. To illustrate this, consider a special case in which $\boldsymbol{u}_R$ and $\boldsymbol{u}_L$ are parallel but $\Delta\boldsymbol{u} \neq 0$. Two directions, streamwise and its normal, are chosen to demonstrate the deficiency of the scheme. These two directions have been considered as the least diffusive directions to compute the flux vector.[5] If θ is the streamwise direction that is close to the rotated upwind direction based on the velocity difference, then $\Delta u_{\perp} = 0$ and thus $\alpha_3 = 0$; if θ is the normal to the streamwise direction that in some cases is close to the direction defined by the pressure gradient, then $\tilde{u}_{\parallel} = 0$ and so is λ_3. In both cases, the shear wave used in the wave model (9) has no contribution to the real shear. In a general case with an arbitrary θ, the situation may be worse and shear waves are not being taken into account properly.

This four-wave model can be modified by adding extra waves as fundamental wave components, such as proposed by Roe.[14] This has been implemented as a five-wave model by Rumsey et al.[12] with one more shear wave that is set at a right angle to the propagating direction so that there is always one effective shear wave. Numerical results in Ref. 12 showed that the five-wave model gave much better solutions than the four-wave model when applied to strong shear

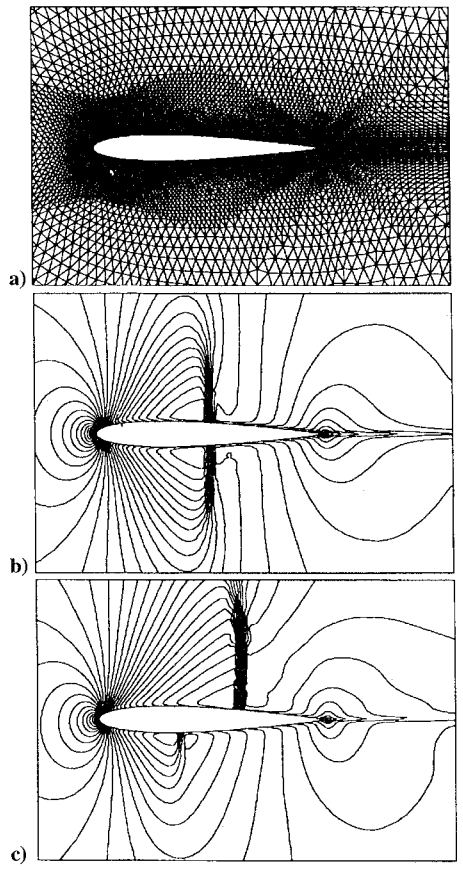

Fig. 7 Semistructured finer grid and computed temperature contours using the standart schemes with M_{inf} = 0.8: a) grid GE-f, b) first-order scheme with α = 0 deg, and c) second-order scheme with α = 1.25 deg.

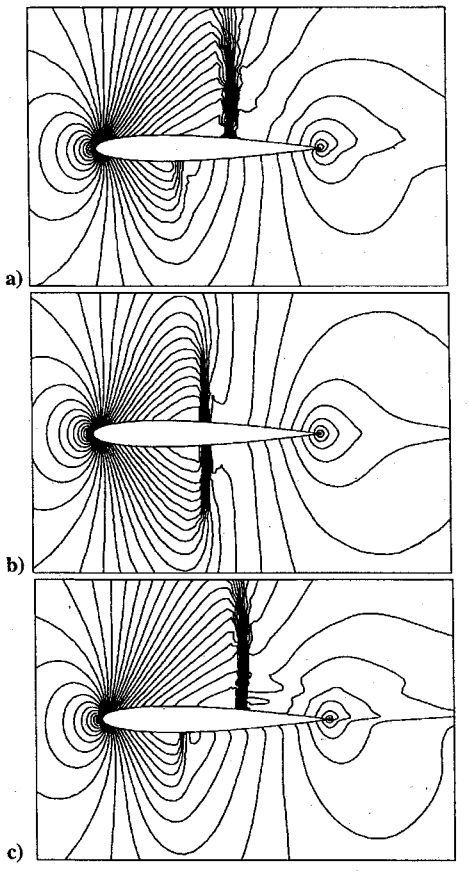

Fig. 8 Computed temperature contours using rotated scheme with M_{inf} = 0.8: a) second-order scheme using grid GE-ust with α = 1.25 deg, b) first-order scheme using grid GE-f with α = 0 deg, and c) second-order scheme using grid GE-f with α = 1.25 deg.

cases including viscous flow computations. Despite its extra dissipation and some robustness problems close to stagnation points,[29] we will use this scheme to illustrate some of the solution improvement. One reason to choose this model is that the shear waves are treated more accurately. The modified expression for all of the terms given and the projection back to the grid normal can be found in Ref. 12 and will not be repeated here.

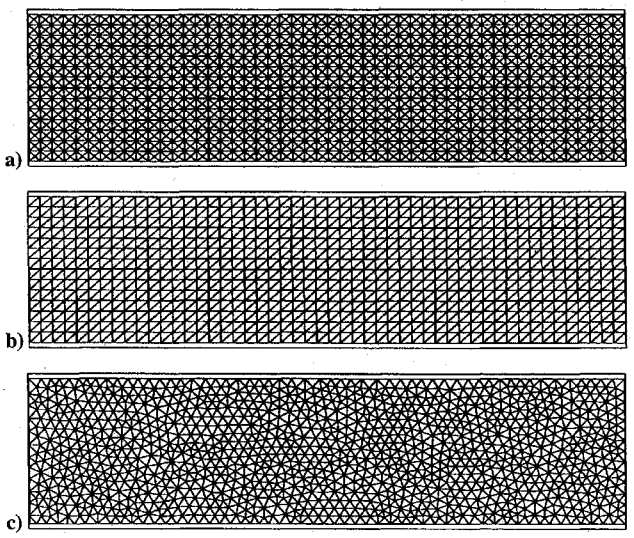

Fig. 9 Uniform computational grids for flat-plate boundary layer with different cut: a) GNS-$_{u1}$, b) GNS-$_{u2}$, and c) GNS-$_{u3}$.

V. Results and Discussions

A set of numerical tests is conducted to verify some of the observations and discussions given in the preceding section. Even though a first-order scheme should not be used for practical computations, it was used for most of the calculations as our present purpose is the study of grid dependency. Second- and third-order schemes are also used to demonstrate their limitation in the improvement of the solution accuracy. Inviscid tests are performed for an NACA0012 airfoil with various grids. Viscous tests are conducted on a flat-plate boundary layer and also on the NACA0012 airfoil.

Inviscid Transonic Flow

A set of tests is performed first for the inviscid flow over an NACA0012 airfoil. The first case is for a flow with 0-deg incidence and Mach number of 0.8. Three triangular coarse grids are employed as shown in Figs. 1a–1c. The grids GE-$_1$ and GE-$_2$ are obtained by cutting two different C-type quadrilateral meshes such that, close to the airfoil surface, the cuts are in different directions. Grid GE-$_3$ is cut from an O type quadrilateral mesh with some skewness such that, close to the surface, the triangles are almost symmetrically placed with respect to the normal of the surface.

A first-order upwind conventional scheme was used for these grids and the Mach isolines are presented in Figs. 2a–2c. It is evident that some boundary-layer like viscous loss along the airfoil surface appears for grids GE-$_1$ and GE-$_2$, whereas there is almost no such behavior for grid GE-$_3$. A much stronger effect is observed on the temperature isolines shown in Figs. 3a–3c even for GE-$_3$. The entropy [which is defined as $p/(\rho^{\gamma}) - 1$] isolines are also plotted in Figs. 4a–4c with increment of 0.003. The maximum entropy values for the three grids GE-$_1$, GE-$_2$, and GE-$_3$ are 0.0552, 0.0477, and 0.0353, respectively. For this problem, it seems that grid GE-$_3$

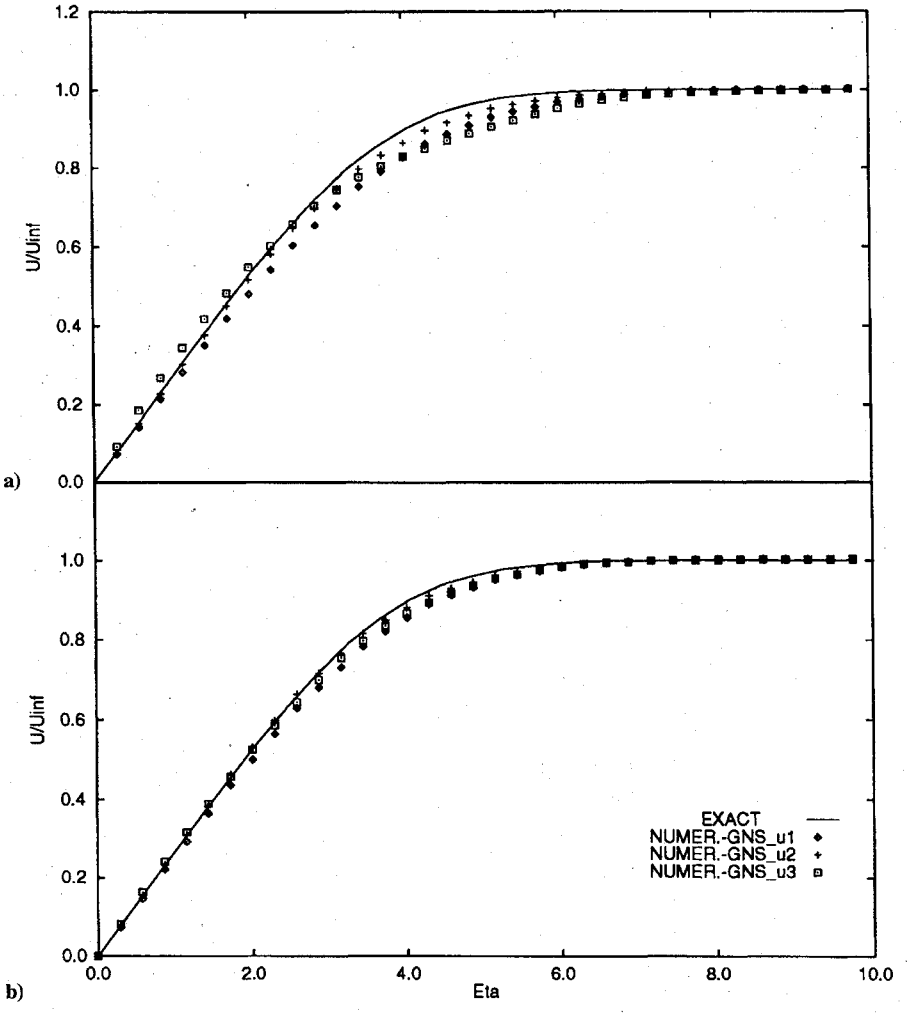

Fig. 10 Velocity profiles obtained using the uniform computational grids: a) standard scheme, and b) rotated scheme.

works better than grid GE_{-2} and both are better than grid GE_{-1}. Grid GE_{-3} has triangles with two-side oblique interfaces and, as a result, the computed solution is superior to the solutions produced by grids GE_{-1} and GE_{-2} that have only one-side oblique triangle interface. However, the shock captured by grid GE_{-3} is more diffused than the others because the grid is not aligned along the shock as it is for the other two grids.

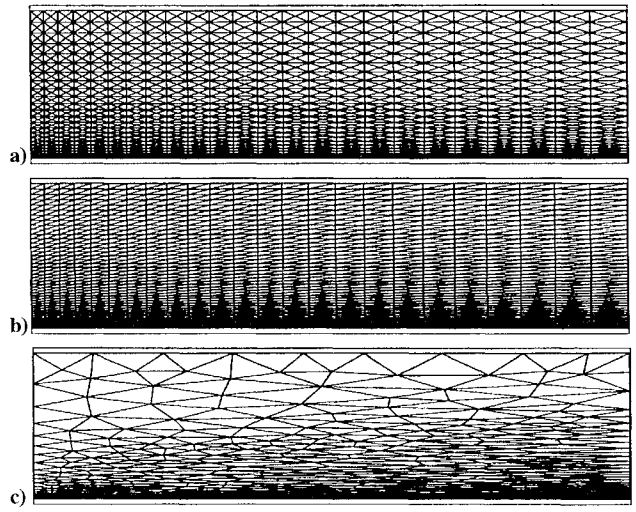

Fig. 11 Stretched computational grids for flat-plate boundary layer with different cut: a) GNS_{-s1}, b) GNS_{-s2}, and c) GNS_{-s3}.

To investigate the possibility of improving the situation, three more computations are conducted and are presented in Figs. 5a–5c using grid GE_{-1}. In this figure, solutions correspond to the isotemperatures using the second-order scheme (Fig. 5a), the third-order scheme (Fig. 5b), and the first-order rotated scheme based on the five-wave model (Fig. 5c),[12] respectively. Comparing these to the solution shown in Fig. 3a, the second-order scheme improved the situation but not much, the third-order scheme does not really yield any improvements over the solution using the second-order scheme, and the rotated upwind scheme almost removed the artificial viscous loss completely. Thus, we may conclude that this kind of solution inaccuracy is more dependent on the grid cutting or grid structure than on the order of the scheme.

A completely unstructured grid (GE_{-ust}) with almost equilateral triangles (Fig. 6a) and a much finer grid (GE_{-f}) with concentration near the airfoil surface (Fig. 7a) were used to verify the same kind of inaccuracy of the inviscid solutions. Both the first-order and second-order standard schemes are used for grid GE_{-ust} with Mach = 0.8 and incidence angle of $\alpha = 1.25$ deg. The isotemperatures are shown in Figs. 6b and 6c. The solution using the second-order rotated upwind scheme is also presented in Fig. 8a for comparison. It is observed that there is almost no viscouslike losses in all of these isolines. For the standard scheme, however, irregular contours are observed, especially with the first-order solution, whereas the rotated one does improve the irregularity as can be seen in front of the weak shock of the lower surface. For the finer grid GE_{-f}, computations using the first-order scheme with $\alpha = 0$ deg and the second-order scheme with $\alpha = 1.25$ deg are conducted, and the isotemperatures are presented in Figs. 7b and 7c and Figs. 8b and 8c without and with the rotated upwinding, respectively. The viscouslike behavior is evident for

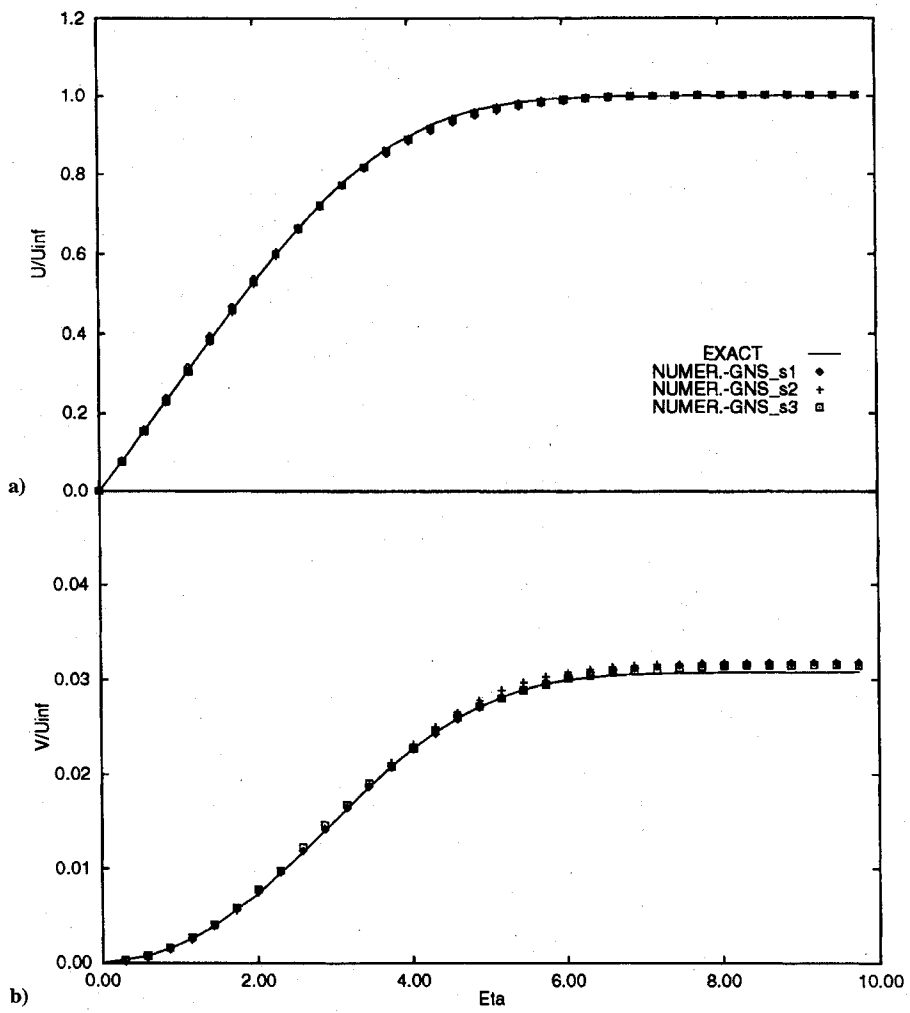

Fig. 12 Velocity profiles obtained using the stretched computational grids and standard scheme: a) longitudinal component and b) transverse component.

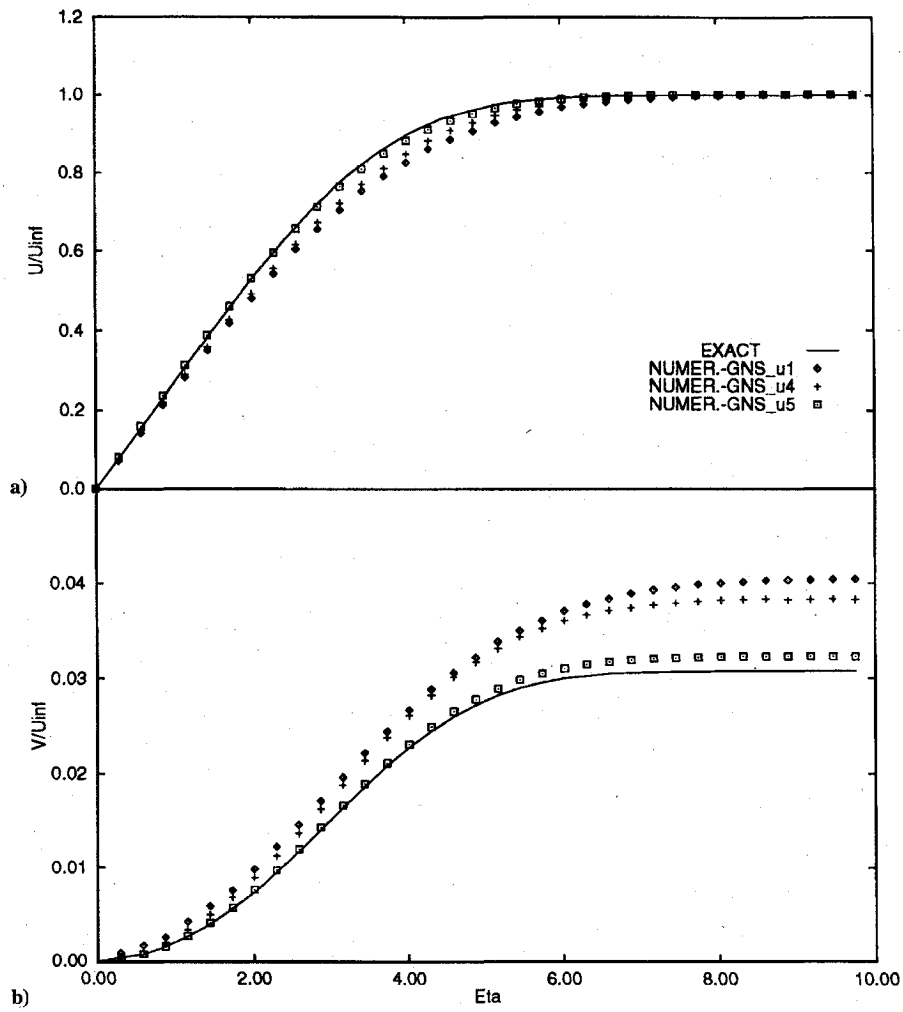

Fig. 13 Velocity profiles obtained using uniform grids with different grid spacing: a) longitudinal component and b) transverse component.

both the first- and second-order results using standard upwinding even for the refined grid but is almost absent in the solutions using rotated upwinding. These tests show that refinement of the grid close to the wall cannot remove the error accumulation, whereas, a much less diffused solution can be obtained by using an unstructured grid that has random interface orientation. The rotated upwind scheme can improve the situation significantly. The improvement for the entropy using the rotated upwind scheme has been discussed and presented in Ref. 12.

These numerical tests indicate that one of the main sources of the viscouslike behavior on the inviscid solutions can be attributed to too large a grid dependency of the upwind scheme based on the grid interface orientation. As a result, unphysical solutions are obtained even in smooth flow regions and not only across discontinuities as just shown.

Flat-Plate Boundary Layer

In the following, the solution of the Navier–Stokes equations with upwinding discretization for the convection term is analyzed. As already discussed, the standard upwinding treatment of the convection term is highly grid dependent and may yield inaccurate solutions near the wall for Euler equations. However, one may expect that for Navier–Stokes equations the viscous fluxes will be dominant near the wall and the upwinding error will have minor effects on the final solution. In fact, it is also important for flows with strong shear.

In this subsection, some computations of viscous flow over a flat plate are presented and compared with analytical solutions.[30] The normal distance away from the plate is scaled as

$$\eta = y\sqrt{u_\infty/\nu_\infty x}$$

where the subscript ∞ represents the property outside the boundary layer. Here, x is the distance measured from the leading edge of the plate. The computations are conducted under the conditions that $Pr = 1.0$ and $\mu = T$. The computational domain is shown in Fig. 9 with a plate length of 2.0 and normal width of 0.5. Analytical inlet boundary conditions are imposed.

The first test is for three different but almost uniform grids (with aspect ratio of 1), shown in Fig. 9, which are symmetrically cut (GNS-$_{u1}$), one-side cut (GNS-$_{u2}$), and totally unstructured (GNS-$_{u3}$), and have 2800, 1400, and 2199 triangles, respectively. The computations were performed with a Mach number of 0.8 and a Reynolds number of 1000 based on unit length. Comparisons of computed and exact velocity profiles that are normalized by the analytical outer layer u-velocity component, using standard and rotated first-order schemes, are presented in Fig. 10 for solutions at station $x = 1.0$. The standard scheme provided quite grid-dependent results. The one-side cut grid (GNS-$_{u2}$), which has fewer triangles than the other two, gave the best solution, probably because the grid lines are more aligned on the streamwise direction. Again, we attribute this grid dependency mainly to the shear wave treatment in the convection upwinding discretization, since the shear waves in the boundary-layer case are stronger than in the inviscid case. From the second part of Fig. 10, it is evident that the rotated five-wave scheme significantly improved the situation, especially in the region $(4 < \eta < 7)$ where the convective fluxes are important compared to the diffusion fluxes.

The second test is for three stretched grids (GNS-$_{s1}$, GNS-$_{s2}$, and GNS-$_{s3}$), shown in Fig. 11, which are prepared in the same way as in the preceding test. They have the same aspect ratio of 50 near the trailing edge and have 2304, 2304, and 820 triangles, respectively. The computed velocity profiles using standard first-order scheme

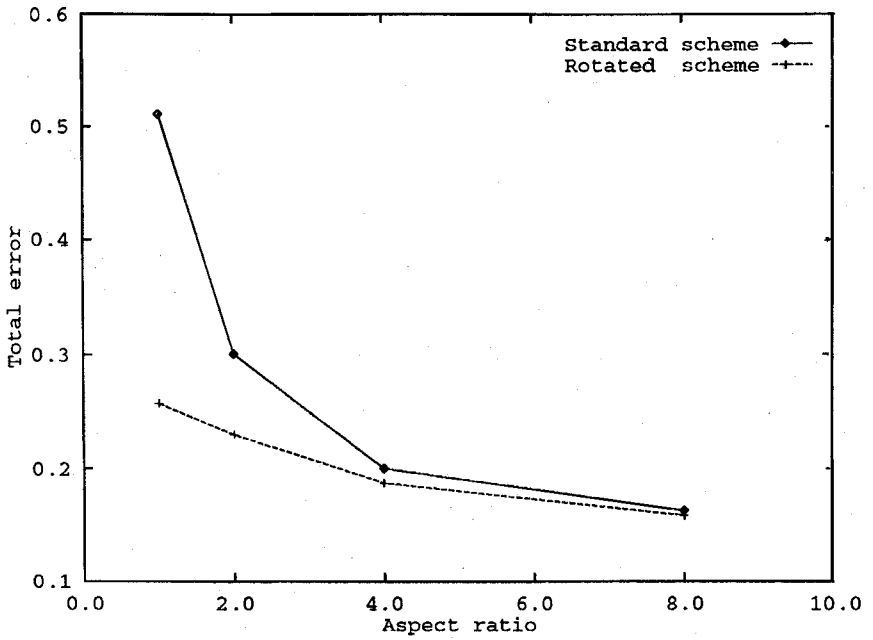

Fig. 14 Total error estimated from the computed and exact velocities with different grid spacing in x direction.

are plotted and compared with the exact solution in Fig. 12. For this set of grids, all of the results, even the one using the unstructured coarsest grid, agree well with the exact solution. In contrast to the earlier test, the grid dependency is not so obvious and the use of rotated upwinding cannot be expected to give better solutions. Actually, as discussed before, the grid dependency is strongly related to the orientation of the grid interface. The stretched grids, like the three shown in Fig. 11, have interfaces that are mainly parallel to the streamwise direction (or perpendicular but with very small side length) inside the boundary layer. In this sense, the three grids have almost the same interface orientation so that the grid dependency of the solutions is minimized.

One could argue that the main effect on the improvement of the solution is the grid refinement in the y direction rather than the interface orientation. A test on two other grids that are similar to grid GNS-$_{u1}$ (uniformly spacing and symmetrically cutting), however, demonstrates that the effect of the grid orientation is a key factor. Grid GNS-$_{u4}$ is obtained by refining grid GNS-$_{u1}$ by a factor of 2 in both the x and y directions; grid GNS-$_{u5}$ is obtained by refining in the y direction while coarsening in x direction by a factor of 2 from grid GNS-$_{u1}$. As a result, grid GNS-$_{u4}$ has four times more triangles than GNS-$_{u1}$ but has the same interface orientation, whereas grid GNS-$_{u5}$ has the same number of triangles as grid GNS-$_{u1}$ and the same grid spacing in the y direction as grid GNS-$_{u4}$. The solution using GNS-$_{u4}$ is still very poor, as shown in Fig. 13, whereas the solution using GNS-$_{u5}$ is much better than the solutions calculated on both grids GNS-$_{u1}$ and GNS-$_{u4}$ (Fig. 13). Several grids were produced by keeping the y spacing as grid GNS-$_{u4}$ while changing the x spacing uniformly. The results are plotted in Fig. 14 in the form of the total error of the velocity ($\sum |U_{\text{comp}} - U_{\text{exact}}|$) vs the aspect ratio of the grids. In these calculations, both the standard and rotated schemes are applied to the same grids with different aspect ratio, which results in different triangle orientation angles. The only difference between the schemes is the treatment of the upwinding term that is strongly dependent on the interface orientation. In Fig. 14, the results using the rotated scheme indicate that the grid aspect ratio has only a small effects at the accuracy, whereas the results using the standard scheme shows large influence of the grid orientation. This clearly demonstrates that the orientation of the edges is an important factor in the grid dependency of the standard scheme.

Viscous Flow over an Airfoil

The last test case concerns the external viscous flow past a NACA0012 airfoil at 0-deg incidence with a Mach number of 0.5

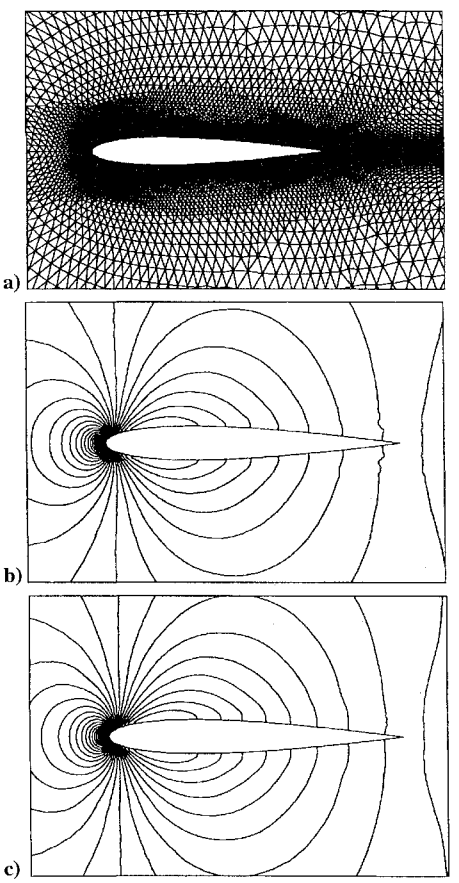

Fig. 15 Semistructured grid around a NACA0012 airfoil and computed pressure contours for viscous flow with $M_{\text{inf}} = 0.5$, $\alpha = 0$ deg, and $Re = 5000$: a) grid GNS-$_{sst}$, b) standard first-order scheme, and c) rotated first-order scheme.

and a Reynolds number of 5000. A semistructured grid with 23,231 triangles (GNS-$_{sst}$ in Fig. 15a) is used for the computation. The aspect ratio of this grid on the airfoil surface is about 100. The pressure contours using both the standard and rotated first-order schemes are depicted in Fig. 15b and 15c. The standard one shows a weak distortion near the trailing edge of the airfoil similar to that reported in Ref. 31 in which a stronger separation occurred. The rotated one

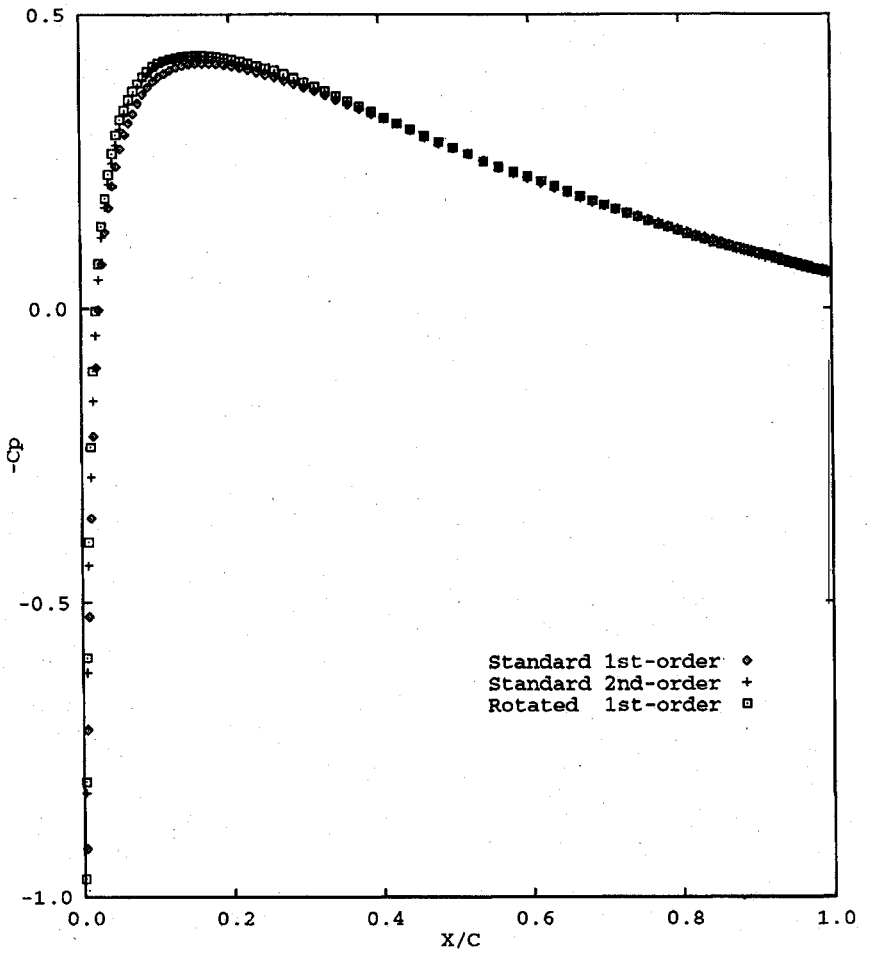

Fig. 16 Computed surface pressure coefficients for viscous flow using grid GNS$_{sst}$ with M_{inf} = 0.5, α = 0 deg, and Re = 5000.

shows much less distorsion, as has been reported and discussed, also in Ref. 12. The computed pressure coefficients C_p using standard first- and second-order schemes as well as the rotated first-order scheme are presented in Fig. 16. It is observed that higher values of $-C_p$ are obtained by the rotated first-order scheme than by the standard first-order scheme and the former ones are very close to the standard second-order result. It seems that the rotated scheme can provide more accurate solution than the standard scheme.

Even if the flow has no separation, however, the distortion on the pressure contours are still grid dependent. As an example, a completely unstructured grid (GNS$_{ust}$ in Fig. 17a) has been made with 20,483 triangles and the aspect ratio is about 50 on the airfoil surface. A closeup of the grid in the trailing edge region is reproduced in Fig. 17b. The grid has a sudden switch from stretched mesh to uniform mesh. The nonstretched mesh may have a strong influence on the solution accuracy. The computation was conducted at 0-deg incidence, Mach number of 0.5, and Reynolds number of 2000. With these parameters, no separation is observed. The pressure contours obtained using the standard first- and second-order schemes and using rotated first-order scheme are depicted in Figs. 18a–18c, respectively. It is evident that the standard first-order scheme produces very distorted pressure contours that reflect the random behavior of the error waves because the grid interfaces there have random orientations. The second-order scheme can improve this kind of behavior, and an even smoother pressure pattern is provided by the rotated first-order scheme with the five-wave model.

It should be pointed out that, for the computations using rotated upwinding scheme, the initial data are imposed by the standard scheme solutions. In all of the inviscid flow test cases, the rotating angle θ was fixed for some number of iterations. After a short period of time, it was frozen for the rest of the calculations to achieve converged solutions, whereas for all of the viscous computations, the

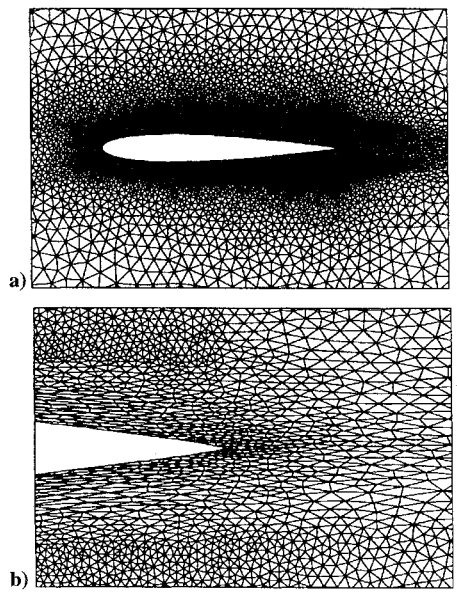

Fig. 17 Completely unstructured grid GNS$_{ust}$: a) around a NACA0012 airfoil and b) closeup near the trailing edge.

rotating angle θ was frozen directly computed from the converged solutions using the standard scheme. It is found that the viscous computations are less sensitive to the readjustment of the rotating angle, but the inviscid computations always need many readjustments of the rotating angle and are very sensitive to the frequency of the adjustment. Once the rotating angle has been frozen, however, the solution convergence is not a difficult issue.

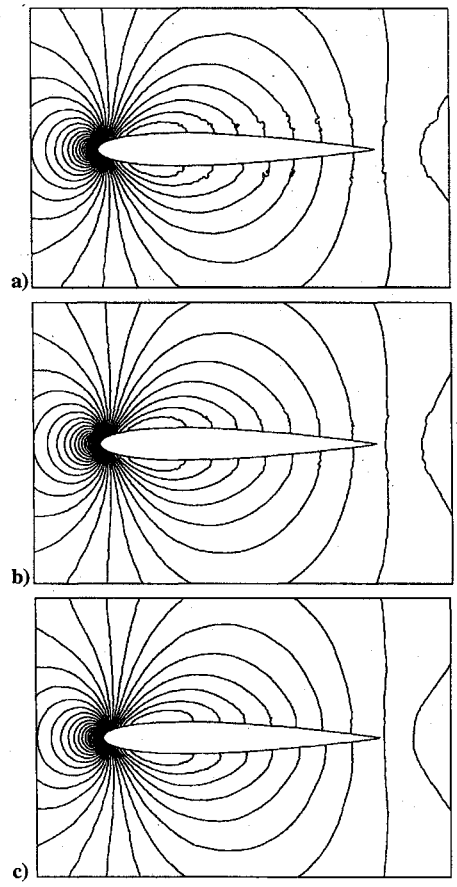

Fig. 18 Computed pressure contours for the viscous flow using grid GNS-$_{ust}$ and parameters $M_{inf} = 0.5$, $\alpha = 0$ deg, and $Re = 2000$: a) standard first-order scheme, b) standard second-order scheme, and c) rotated first-order scheme.

VI. Concluding Remarks

From the numerical investigations conducted in this paper, it is felt that the standard first-order upwind scheme of Roe in two space dimensions is so grid dependent that unphysical numerical solutions can be produced even for regularly structured triangular meshes. It is very hard to conclude that completely unstructured meshes can provide better solutions although sometimes they do. Management of the grid to improve the solution may not always be practical and may not even be possible in some cases. HOR can generally improve the solution accuracy, but has its own limitations. Really multidimensional grid-independent schemes can be developed taking into account more physical aspects of the problems. It is worth noting that the rotated upwinding with a five-wave model can repair, to some degree, the unphysical solutions. The convergence performance and robustness of this method, however, need to be improved.

Acknowledgments

The financial support provided by the National Science and Engineering Research Council of Canada through operational grants is gratefully acknowledged. The authors wish to thank F. Mokhtarian of Canadair for numerous discussions and for providing us with some grids used for the computations. The authors also thank the reviewers for their comments.

References

[1]Godunov, S. K., "Finite-Difference Method for Numerical Computation of Discontinuous Solutions of the Equations of Fluid Dynamics," *Matema. Sbornik.*, Vol. 47, No. 3, 1959, pp. 271–306.

[2]Roe, P. L., "Approximate Riemann Solvers, Parameter Vectors, and Difference Schemes," *Journal of Computational Physics*, Vol. 43, No. 2, 1981, pp. 357–372.

[3]Paraschivoiu, M., Trépanier, J.-Y., Reggio, M., and Camarero, R., "A Conservative Dynamic Discontinuity Tracking Algorithm for the Euler Equations," AIAA Paper 94-0081, Jan. 1994.

[4]Parpia, I. H., and Parikh, P., "A Solution-Adaptive Mesh Generation Method with Cell-Face Orientation Control," AIAA Paper 94-0416, Jan. 1994.

[5]Liou, M.-S., "An Extended Lagrangian Method," AIAA Paper 93-3305, July 1993.

[6]Yee, H. C., "A Class of High-Resolution Explicit and Implicit Shock-Capturing Methods," Computational Fluid Dynamics, Von Kármán Inst., VKI Lecture Series 1989-04, Rhôde Saint Genèse, Belgium, March 1989.

[7]Barth, T. J., "Aspects of Unstructured Grids and Finite-Volume Solvers for the Euler and Navier–Stokes Equations," Computational Fluid Dynamics, Von Kármán Inst., VKI Lecture Series 1994-05, Rhôde Saint Genèse, Belgium, March 1994.

[8]Vankeirsbilck, P., "Application of Solution Adaptive Meshes and Multigrid Methods for the Computation of Viscous Compressible Flows," Von Kármán Inst., VKI Contract Rept., Rhôde Saint Genèse, Belgium, Sept. 1991.

[9]Aftosmis, M., Gaitonde, D., and Tavares, T. S., "On the Accuracy, Stability and Monotonicity of Various Reconstruction Algorithms for Unstructured Meshes," AIAA Paper 94-0415, Jan. 1994.

[10]Davis, S. F., "A Rotationally Biased Upwind Difference Scheme for the Euler Equations," *Journal of Computational Physics*, Vol. 56, No. 1, 1984, pp. 65–92.

[11]Levy, D. W., Powell, K. G., and van Leer, B., "An Implementation of a Grid-Independent Upwind Scheme for the Euler Equations," AIAA Paper 89-1931, June 1989.

[12]Rumsey, C. P., van Leer, B., and Roe, P. L., "A Multidimensional Flux Function with Applications to the Euler and Navier–Stokes Equations," *Journal of Computational Physics*, Vol. 105, No. 2, 1993, pp. 306–323.

[13]Kontinos, D. A., and McRae, D. S., "Rotated Upwind Strategies for Solution of the Euler Equations," AIAA Paper 94-0079, Jan. 1994.

[14]Roe, P. L., "Discrete Models for the Numerical Analysis of Time-Dependent Multidimensional Gas Dynamics," *Journal of Computational Physics*, Vol. 63, No. 2, 1986, pp. 458–476.

[15]Parpia, I. H., and Michalek, D. J., "A Nearly-Monotone Genuinely Multidimensional Scheme for the Euler Equations," AIAA Paper 92-0325, Jan. 1992.

[16]Rudgyard, M., "Multidimensional Wave Decompositions for the Euler Equations," Computational Fluid Dynamics, Von Kármán Inst., VKI Lecture Series 1993-04, Rhôde Saint Genèse, Belgium, March 1993.

[17]Deconinck, H., Hirsch, C., and Peuteman, J., "Characteristic Decomposition Methods for the Euler Equations," *Lecture Notes in Physics*, Vol. 6, 1986, pp. 216–221.

[18]Van Ransbeeck, P., and Hirsch, C., "New Upwind Dissipation Models with a Multidimensional Approach," AIAA Paper 93-3304, July 1993.

[19]Deconinck, H., "Analysis of Wave Propagation Properties for the Euler Equations in two Space Dimensions," Computational Fluid Dynamics, Von Kármán Inst., VKI Lecture Series 1994-05, Rhôde Saint Genèse, Belgium, March 1994.

[20]Paillere, H., Carette, J.-C., and Deconinck, H., "Multidimensional Upwind and SUPG Methods for the Solution of the Compressible Flow Equations on Unstructured Grids," Computational Fluid Dynamics, Von Kármán Inst., VKI Lecture Series 1994-05, Rhôde Saint Genèse, Belgium, March 1994.

[21]Barth, T. J., and Jespersen, D. C., "The Design and Application of Upwind Schemes on Unstructured Meshes," AIAA Paper 89-0366, Jan. 1989.

[22]Glaister, P., "A Shock-Capturing Scheme for Body-Fitted Meshes," *International Journal for Numerical Methods in Fluids*, Vol. 8, No. 9, 1988, pp. 1095–1105.

[23]Barth, T. J., "Recent Developments in High Order k-Exact Reconstruction on Unstructured Meshes," AIAA Paper 93-0668, Jan. 1993.

[24]Barth, T. J., and Frederickson, P. O., "High Order Solution of the Euler Equations on Unstructured Grids Using Quadratic Reconstruction," AIAA Paper 90-0013, Jan. 1990.

[25]Venkatakrishnan, V., "On the Accuracy of Limiters and Convergence to Steady State Solutions," AIAA Paper 93-0880, Jan. 1993.

[26]Zhang, X. D., Trépanier, J.-Y., Benmeddour, A., and Camarero, R., "Studies of Navier–Stokes Computation on Unstructured Meshes," *Proceeding of the 2nd Conference of the CFD Society of Canada*, CFD Society of Canada, Toronto, ON, Canada, 1994, pp. 123–130.

[27]Zhang, X. D., Trépanier, J.-Y., Reggio, M., and Camarero, R., "Time-Accurate Local Time Stepping Method Based on Flux Updating," *AIAA Journal*, Vol. 32, No. 9, 1994, pp. 1926–1929.

[28]Currie, T. C., "A Simple Multigrid Procedure for Explicit Time-Marching on Unstructured Grids," *Proceedings of the AIAA 11th Computational Fluid Dynamics Conference*, AIAA, Washington, DC, 1993, pp. 1033, 1034.

[29]Roe, P. L., "Multidimensional Upwinding: Motivation and Concepts," Computational Fluid Dynamics, Von Kármán Inst., VKI Lecture Series 1994-05, Rhôde Saint Genèse, Belgium, March 1994.

[30]Schlichting, H., *Boundary-Layer Theory*, 7th ed., McGraw–Hill, New York, 1979, pp. 340–352.

[31]Venkatakrishnan, V., "Viscous Computations Using a Direct Solver," *Computers and Fluids*, Vol. 18, No. 2, 1990, pp. 191–204.